Aerothermal characterization of the CALLISTO vehicle during descent

Tobias Ecker⋆*, Moritz Ertl*⋆*, Josef Klevanski*⋆*, Sven Krummen*‡ *and Etienne Dumont*‡
German Aerospace Center (DLR)
⋆ *Institute of Aerodynamics and Flow Technology*
Bunsenstr. 10, 37073 Göttingen, Germany
‡*Institute of Space Systems*
Robert-Hooke-Strasse 7, 28359 Bremen, Germany
tobias.ecker@dlr.de · moritz.ertl@dlr.de · josef.klevanski@dlr.de
sven.krummen@dlr.de · etienne.dumont@dlr.de

Abstract

Aerothermal loads are a design driving factor during launcher development as the thermal loads directly influence TPS design and trajectory. Recent developments in reusable launch vehicles (RLV) (e.g. SpaceX, Blue Origin) have added the dimension of refurbishment to the challenges the thermal design must consider. For disposable launchers the heat flux due to base heating during ascent needs to be considered for aft thermal protections system (TPS) and structural design. With the current European long term strategy[1] moving towards a reusable first stage - aerothermal loads may significantly change. The CALLISTO vehicle is a flight demonstrator for future reusable launcher stages and their technologies. The program involves three countries and their space organizations: CNES for France, DLR for Germany and JAXA for Japan. The first tests will be conducted in 2024 from CSG, Europe's Spaceport. The challenge is to develop, all along the project, the skills of the partners. This know-how includes products and vehicle design, ground segment set up, and post-flight operations for vehicle recovery then reuse [2–5]. For the CALLISTO vehicle the highest heat fluxes are mainly due to heating from hot exhaust gases and heated air in proximity of the aft bay and on the exposed structures like legs and fins. The development of the plume extension is different for the considered re-entry, when compared to Falcon 9, or the studies presented in [6–8]. As shown by Dumont et al.[9] the plume remains relatively concentrated at the aft end of the vehicle due to high atmospheric pressure and only very low fractions of actual exhaust gas species enclosing the vehicle. In the current study we conducted computational fluid dynamics (CFD) studies in order to determine the aerothermal loads on the vehicle during descent through the landing approach corridor for both phase B and phase C aeroshapes. The database development for vehicle phase B and phase C are described in detail and analyzed for some of the most prominent interfaces. The final phase C database presented allows interpolation of interface heatfluxes for the entire flight domain (M, ρ) at varying angle of attack (between 180 deg and 160 deg). Further the sensitivity of the plume-vehicle interaction to angle of attack, chemistry, thrust vector deflection and engine throttling are investigated for a critical Mach number indicating further area of improvement for future databases.

1. Introduction

Aerothermal loads are a design driving factor during launcher development as the thermal loads directly influence TPS design and trajectory. Recent developments in reusable launch vehicles (RLV) (e.g. SpaceX, Blue Origin) have added the dimension of refurbishment to the challenges the thermal design must consider.

For classical disposable launchers like the Ariane 5 [10] and 6, the TITAN 3C [11], but also the spaceshuttle launch and reentry [12], the heat flux due to base heating during ascent needs to be considered for aft thermal protections system (TPS) and structural design. In all these configurations the use of solid rocket boosters lead to a significant increase in heat flux due to plume radiation. With the current European long term strategy[1, 13] moving from the LH2/LOX powered Vinci and Vulcain 2.1 on Ariane 6, supported by solid rocket boosters, to a single engine concept (Prometheus [14, 15]) based on LCH4/LOX with (possibly*) no solid rocket boosters on a future European launcher -

*Presentation by Jean-Marc Astorg, Conference Palais de la Decouverte, 31 May 2018

aerothermal loads may significantly change.

The CALLISTO vehicle is a flight demonstrator for future reusable launcher stages and their technologies. The program involves three countries and their space organizations: CNES for France, DLR for Germany and JAXA for Japan. The first tests will be conducted in 2024 from CSG, Europe's Spaceport. The challenge is to develop, all along the project, the skills of the partners. This know-how includes products and vehicle design, ground segment set up, and post-flight operations for vehicle recovery then reuse[2–5].

For the CALLISTO vehicle the highest heat fluxes are mainly due to heating from hot exhaust gases and heated air in proximity of the aft bay and on the exposed structures like legs and fins. The development of the plume extension is different for the considered re-entry, when compared to Falcon 9, or the studies presented in [7, 16, 17]. As shown by Dumont et al.[9] the plume remains relatively concentrated at the aft end of the vehicle due to high atmospheric pressure and only very low fractions of actual exhaust gas species enclosing the vehicle. In the current study we conducted computational fluid dynamics (CFD) studies in order to determine the aerothermal loads on the vehicle during descent through the landing approach corridor. The CALLISTO general flight profile, vehicle configuration, vehicle aeroshape evolution and the relevant thermal interfaces as well as the flight domain and its changes from phase B to C are described in detail. The engine model and thermodynamic modeling approach are described and applied to preparatory 2D studies of the engine plume .The database development for vehicle phase B and phase C aeroshapes are described and analyzed for some of the most prominent interfaces. Further the sensitivity of the plume-vehicle interaction to angle of attack, chemistry, thrust vector deflection and engine throttling are investigated. For the purpose of this study the main focus is on the closed leg configuration, more details for the configuration right before touchdown can be found in Ertl et al.[18].

2. CALLISTO configurations, aeroshape and flight domain

2.1 General CALLISTO flight profile

The CALLISTO vehicle and flight experiment aim to demonstrate the technologies and capabilities to realize a VTVL first stage launcher. The basic vehicle architecture is outlined in figure 1. As an experimental vehicle, flight conditions are similar for a certain flight phases but not the same as the ones encountered by full scale VTVL first stage launcher (e.g. Falcon 9). Differences arise in altitude, maximum Mach number and realizable trajectory/flight parameters. The main difference is the lack of a supersonic retro-propulsion phase as encountered in [6, 8].

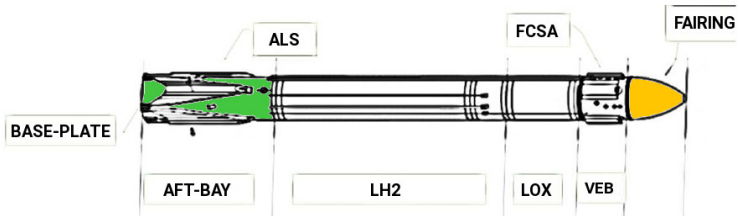

Figure 1: Overview of CALLISTO vehicle architecture (adapted from [19]).

The altitude and Mach number during flight, as well as heat fluxes in terms of Nusselt number on selected interfaces (as marked in figure 1) for a representative trajectory [19] are shown in figure 2 based on preliminary 2D calculations. The Nusselt number is defined as:

$$Nu = \frac{qL}{k * (T_c c - T_\infty)} \tag{1}$$

where q is the heat flux, L the characteristic length (d = 1.1m), k the thermal conductivity of air and T_{cc} the combustion chamber temperature and T_∞ the wall temperature.

It can be seen that there are two main differences when compared to a classical expendable launcher: First, asides from the heat flux on the baseplate which is due to convective base heating, the heat flux due to aerodynamic heating is minimal. This is due to the low supersonic and subsonic Mach numbers during the ascent and ballistic descent. The heat flux on the fairing of Ariane 5 is of the order of 10-20 kW/m^2, while for the CALLISTO vehicle it is negative until the retro-boost manoeuvre. The second difference is the occurrence of high heat fluxes during the retro boost manoeuvre, leading to thermal loads 2-4 times higher than occurring during forward flight. More information on the CALLISTO flight profile and demonstration flight objectives can be found in [5, 20].

During flight four main flight regimes are present: powered vehicle forward flight, ballistic vehicle forward flight, ballistic vehicle return flight and vehicle retro boost during return flight. During the actual flight various vehicle attitudes (angle of attack, roll angle etc.) are possible. During forward flight the hot exhaust gases are entrained into the recirculation zone at the base of the vehicle, leading to high convective heat fluxes during powered ascent. The ballistic phases have no significant aerothermal implications due to the low Mach numbers of CALLISTO flight profile. This flight regime will be more important for large scale demonstrators like THEMIS which will reach higher Mach numbers and altitudes at a full scale flight envelope [13]. The interaction between exhaust plume, the oncoming air and the vehicle leads to significantly higher heat fluxes, making this the flight phase with the highest thermal loads.

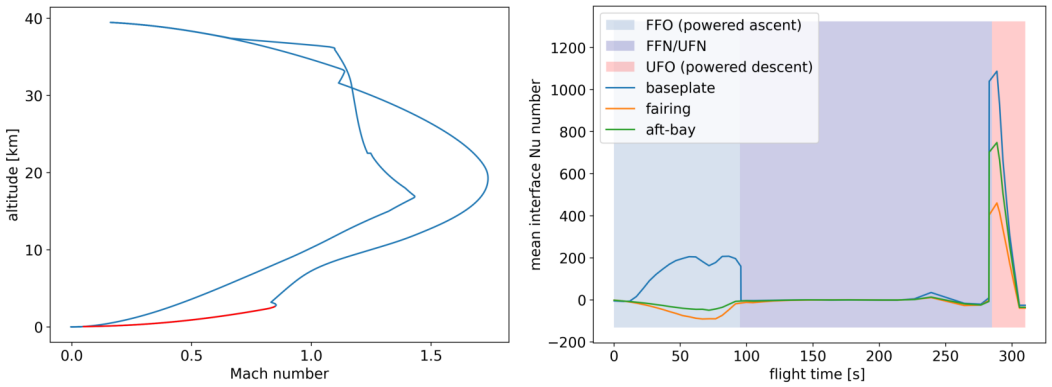

(a) Representative trajectory. Red line marks the powered descent phase.

(b) Nu number on fairing, aft-bay and baseplate during example flight profile. (based on 2D model, T_w = const. = 300 K)

Figure 2: Representative CALLISTO flight profile and preliminary aerothermal characteristics (early Phase A).

2.2 CALLISTO vehicle configurations

During the descent trajectory multiple configurations with regards to vehicle external parts (FCS/A: aerodynamic control surfaces, landing legs) and ground influence exists. Due to the multitude of required calculations, calculations of non critical points of the flight domain are conducted by by using a simplified 2D-axisymmetric outer mold line. An overview of the considered configurations is given in Table 1.

Table 1: Considered configurations.

Configuration	FCS/A status	Legs status	Engine status	Ground status
UFO (2D)	NA	folded	active	NA
UFO	unfolded	folded	active	NA
UUO	unfolded	unfolded	active	NA
UUO ground	unfolded	unfolded	active	on ground

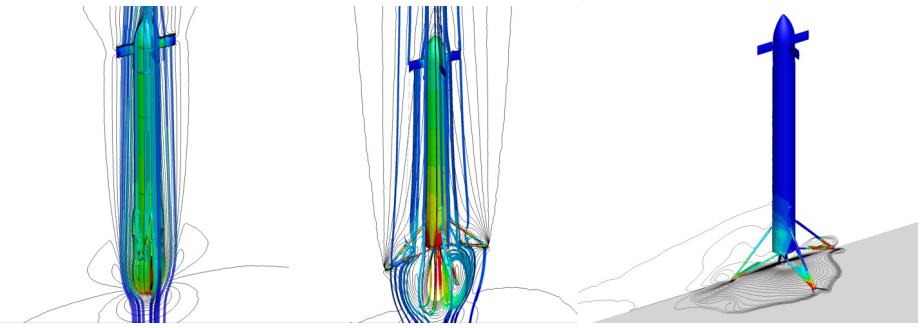

(a) UFO flight

(b) UUO flight

(c) UUO on ground

Figure 3: Applicable CAL1B 3D configurations.

2.3 CALLISTO aeroshape evolution

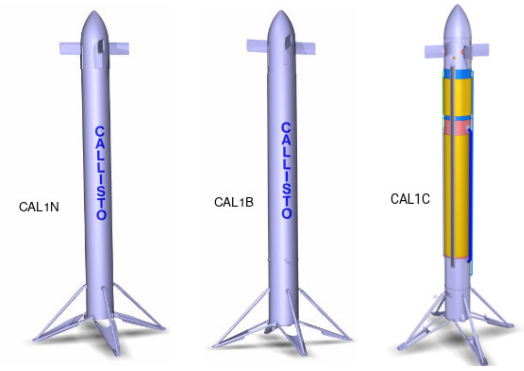

Figure 4: CALLISTO aeroshape evolution

During the project the CALLISTO aeroshape has changed in various ways. A comparison of previous outer mold lines with the shape CAL1B (phase B shape) can be found in [19]. From Phase B onwards the shape changes were mostly limited to detailed design of legs, cable ducts and piping as well as changes due to TPS application and product design. For this paper only aeroshapes CAL1B and CAL1C are considered. The aeroshape evolution and related aerodynamic properties are further detailed in [21].

2.4 CALLISTO thermal interfaces

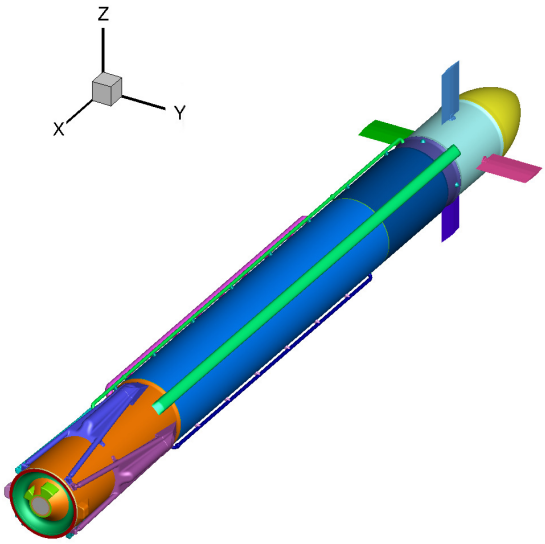

Figure 5: CALLISTO CAL1C vehicle: overview of thermal and aerodynamic interfaces.

For use in the CALLISTO design process and loads definition, thermal interfaces (tanks, legs, etc..) for the entire vehicle were defined. While the CAL1B aeroshape had 15 thermal interfaces, the number of interfaces for the CAL1C aeroshape had more than 50 thermal interfaces. The number of interfaces varies by configuration, with more interfaces being present for the legs open (e.g. UUO) configuration. A graphic of the thermal interfaces is shown in figure 5. The fairing and legs assemblies have multiple thermal interfaces not pictured here which are described more in detail in references [22] and [18]. Additional zoning of interfaces is possible during post-processing based on user needs.

3. CFD Solver and models

All numerical investigations in the framework of the present study were performed with the hybrid structured/unstructured DLR Navier-Stokes solver TAU[23], which is validated for a wide range of steady and unsteady sub-, trans- and hy-

personic flow cases. The TAU code is a second order finite-volume solver for the Euler and Navier-Stokes equations in the integral form using eddy-viscosity, Reynolds-stress or detached- and large eddy simulation for turbulence modeling. The AUSMDV flux vector splitting scheme was applied together with MUSCL gradient reconstruction to achieve second order spatial accuracy.

3.1 Engine conditions

The Reusable Sounding Rocket (RSR) engine used for CALLISTO is developed by JAXA in cooperation with Mitsubishi Heavy Industries (MHI) and is based on LOX/LH_2 fuel. The RSR engine uses an expander bleed cycle, is restartable and throttable between 40 and 100 % nominal thrust [24]. Further studies demonstrated an increased throttle range between 21 and 109 % [25]. By-passing the turbopumps allows operation in "idle mode" [5]. A summary on the RSR engine which will be used in a modified version for CALLISTO can be found in [26]. For CALLISTO operation up to 110 % thrust level is planned. All calculations or CAL1B are at nominal thrust level, while for CAL1C based data 110% thrust level was assumed (see table 2, unless specified otherwise).

Table 2: Engine conditions [24, 26, 27]. ND: not disclosed.

Condition	**110 %**	**nominal (100 %)**	**40 %**	**20 %**	**idle**
Thrust	44 kN	40 kN	16 kN	8 kN	ND
Specific impulse (sea level)	ND	320 s	270 s	ND	ND
Mixture ratio	ND	6	6.2	ND	ND
Chamber pressure	ND	34 bar	16 bar	ND	ND
Chamber temperature	approx. 3500 K	ND	ND	ND	ND

3.2 Chemistry

The rate change of species due to post combustion can be modeled using a finite rate chemistry approach. The rate at which each species changes during a chemical process is determined from the chemical reactions as [28]:

$$\omega_s = M_s \sum_r (\beta_s^r - \alpha_s^r) \left[k_r^f \prod_s (n_s)^{\alpha_s^r} - k_r^b \prod_s (n_s)^{\beta_s^r} \right]$$

where α_s^r and β_s^r are the stoichiometric coefficients for the educt and product for reaction r respectively, k_r^f and k_r^b the forward and backward reaction rate for reaction r respectively, n_s is the molar density and M_s is the molar mass of species s. k_r^f and is the forward reaction rate according to the Arrhenius law

$$k = A\, T^n \exp\left(-\frac{E_a}{RT}\right)$$

where A is the pre-exponential factor, n is the temperature exponent and E_a is the activation energy. The rate constants k_b^f for the reverse reactions are evaluated from the equilibrium constants.

3.3 Thermo-chemical models for retro-propulsion

The influence of plume chemistry and turbulence model was investigated during an early phase B study. For an approximate 2D configuration based on CAL1B geometry[19] the influence of the Spalart-Allmaras, k-ω SST and RSM turbulence models were investigated along with plume chemistry based on finte rate chemistry models. The model used here is the reduced Jachimowsky mechanism [29].

The chemistry as well as the thermodynamic properties of the engine exhaust plume can be modeled in various ways. An overview of the possible modeling approaches is given in table 3. In all cases it is assumed that chemical equilibrium is present at engine chamber conditions. Equilibrium species concentrations and temperature are calculated using NASA CEA [30] for the engine conditions given in table 2. Except for when full chemistry is considered, air is assumed to be a thermally perfect gas of frozen composition (Y_{N_2}: 0.752, Y_{O_2}: 0.2315, Y_{Ar}: 0.0128, Y_{CO_2}: 3.5e-5). Both thermodynamic properties and transport properties are converted from the CEA[30] databases for use in DLR TAU.

Table 3: Possible chemistry models. (FR: frozen, EQ: chemical equilibrium, NEQ: chemical non equilibrium modelled using finite rate chemistry)

Name	**chamber (CC)**	**nozzle (N)**	**plume**	**thermodynamic modell**
constant gamma gas (FR-γ)	EQ	FR	FR	perfect gas (γ = 1.14)
frozen gas (FR-CC)	EQ	FR	FR	2 thermally perfect gas mixtures
frozen gas (FR-N)	EQ	EQ	FR	2 thermally perfect gas mixtures
full chemistry (NEQ-CC)	EQ	NEQ	NEQ	mixture thermally perfect gases

Table 4: Gerlinger reaction mechanism. Units in cm, mol, cal, s.

				Rate Constants		
No.	Reaction			A	n	E_a
1	$H_2 + O_2$	$\rightleftharpoons$	$HO_2 + H$	1.0000e+14	0.00	5.6000e+04
2	$H + O_2$	$\rightleftharpoons$	$HO + O$	2.6000e+14	0.00	1.6800e+04
3	$O + H_2$	$\rightleftharpoons$	$HO + H$	1.8000e+10	1.00	8.9000e+03
4	$HO + H_2$	$\rightleftharpoons$	$H_2O + H$	2.2000e+13	0.00	5.1500e+03
5	$2\,HO$	$\rightleftharpoons$	$H_2O + O$	6.3000e+12	0.00	1.0900e+03
6[a]	$H + HO + M$	$\rightleftharpoons$	$H_2O + M$	2.2000e+22	-2.00	0.0000e+00
7[b]	$2\,H + M$	$\rightleftharpoons$	$H_2 + M$	6.4000e+17	-1.00	0.0000e+00
8[c]	$H + O + M$	$\rightleftharpoons$	$HO + M$	6.0000e+16	-0.60	0.0000e+00
9[d]	$H + O_2 + M$	$\rightleftharpoons$	$HO_2 + M$	2.1000e+15	0.00	-1.0000e+03
10	$HO_2 + H$	$\rightleftharpoons$	$2\,HO$	1.4000e+14	0.00	1.0800e+03
11	$HO_2 + H$	$\rightleftharpoons$	$H_2O + O$	1.0000e+13	0.00	1.0800e+03
12	$HO_2 + O$	$\rightleftharpoons$	$O_2 + HO$	1.5000e+13	0.00	9.5000e+02
13	$HO_2 + HO$	$\rightleftharpoons$	$H_2O + O_2$	8.0000e+12	0.00	0.0000e+00
14	$2\,HO_2$	$\rightleftharpoons$	$H_2O_2 + O_2$	2.0000e+12	0.00	0.0000e+00
15	$H + H_2O_2$	$\rightleftharpoons$	$H_2 + HO_2$	1.4000e+12	0.00	3.6000e+03
16	$O + H_2O_2$	$\rightleftharpoons$	$HO + HO_2$	1.4000e+13	0.00	6.4000e+03
17	$HO + H_2O_2$	$\rightleftharpoons$	$H_2O + HO_2$	6.1000e+12	0.00	1.4300e+03
18[e]	$H_2O_2 + M$	$\rightleftharpoons$	$2\,HO + M$	1.2000e+17	0.00	4.5500e+04
19	$2\,O + M$	$\rightleftharpoons$	$O_2 + M$	6.0000e+13	0.00	-1.8000e+03

[a] H_2O = 6.0
[b] H_2 = 2.0, H_2O = 6.0
[c] H_2O = 5.0
[d] H_2 = 2.0, H_2O = 16.0
[e] H_2O = 15.0

3.4 Retro-propulsion plumes

In order to study the influence of turbulence modeling and post combustion within the plume, a brief 2D study on a subsonic retropropulsion flow field was conducted. An overview of the calculation case matrix for this study is given in table 5, single equation, two-equation and the 5 equation RSM turbulence models were considered. While for supersonic retro-propulsion, the plume shape seems to be somewhat less sensitive to the turbulence modeling[6, 8] larger differences appear for the subsonic case. The results are visualized for the plume temperature in figure 6. The plume shape and temperature distribution shows that both post-combustion and turbulence model can play a large role in the (subsonic) retro-propulsion plume flow field. However, compared to Kerosene or Methane, post-combustion is limited for hydrogen fueled engines. For the centerline both the temperature and OH mass fraction as an indicator of post combustion are shown in figure 7. Based on the temperature distribution on the centerline, the plume length can be between two to four reference diameters (d=1.1m), with the two equation turbulence models and the RSM turbulence model predicting a longer plume length. Naturally the OH mass fraction is highest in the stagnation region between plume and oncoming flow. The temperature increase on the centerline is approximately 500 K when compared to the frozen gas model. Regardless of this outcome, the Spalart-Allmaras (SA) turbulence model[31] is used as the baseline for all future calculations due to its inherent robustness for application in large flight parameter spaces.

Table 5: Case matrix.

Turbulence Modell	**FR-γ**	**FR-CC**	**FR-N**	**NEQ-CC**
Spalart-Allmaras (SA)		x		x
kω-SST		x		x
Reynolds Stress Modell (RSM) Wilcox		x		x
Reynolds Stress Modell (RSM) SSG				x

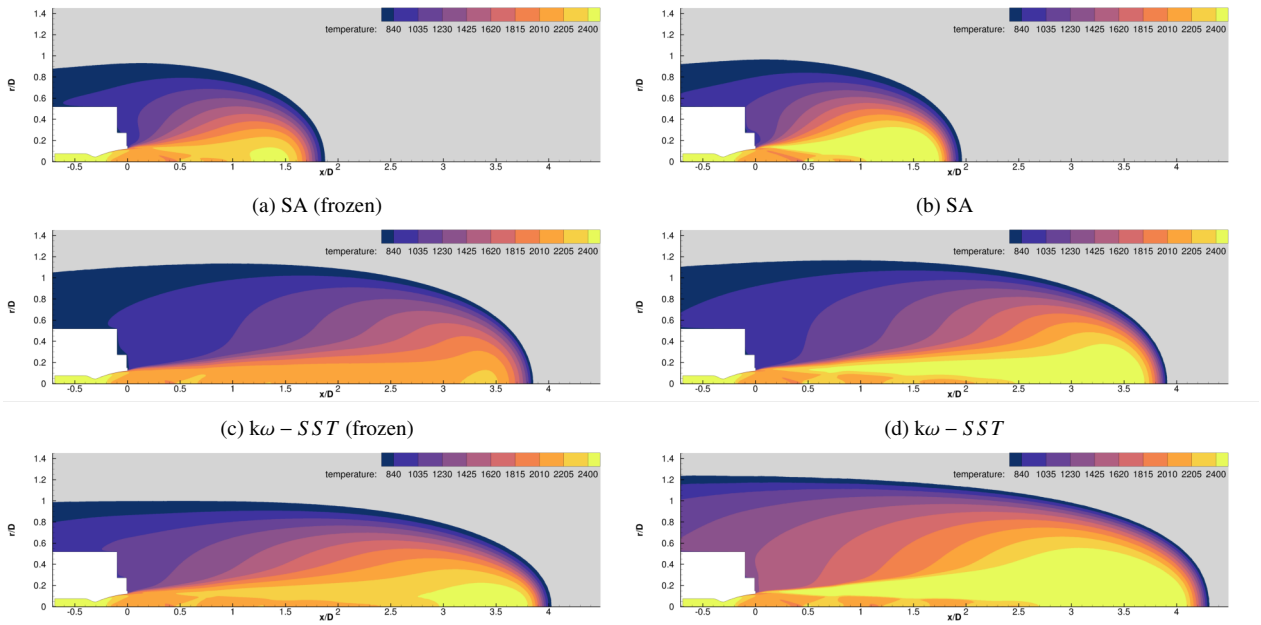

(a) SA (frozen)

(b) SA

(c) k$\omega - SST$ (frozen)

(d) k$\omega - SST$

(e) RSM (frozen)

(f) RSM

Figure 6: Comparison of different chemical and thermodynamic models for the exhaust gas and Spalart-Allmaras turbulence model.

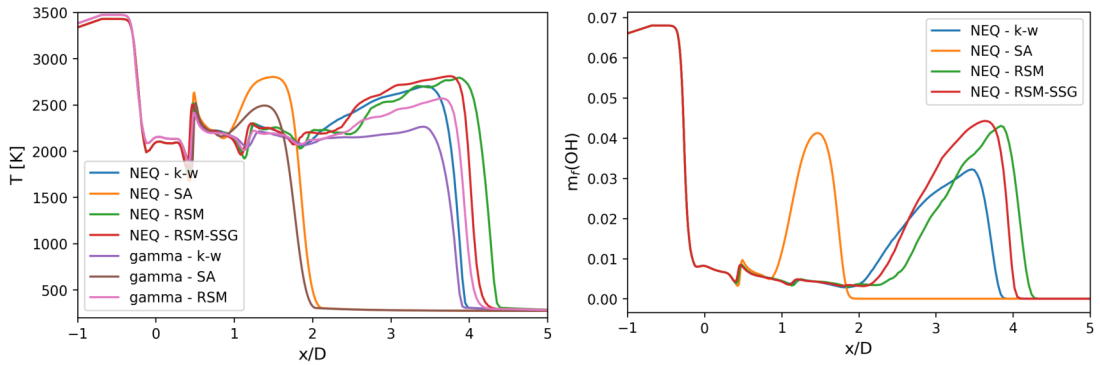

(a) plume centerline temperature

(b) plume centerline OH mass fraction

Figure 7: Comparison of Spalart-Allmaras, k-w SST and RSM turbulence model with full chemistry.

4. Aerothermal database for systems engineering

In this section we describe the general approach to generating aerothermal data for the CALLISTO aerothermal databases, the applied CFD models, as well as general sensitivities of the aerothermal loads to parameters like angle of attack.

4.1 CFD Solver settings and grids

For all calculations contained within the aerothermal database, the Spalart–Allmaras[31] (SA) one-equation eddy viscosity model in the original implementation without the trip term and the turbulence suppression term in laminar regions was used[31, 32]. This SA model is essentially a low-Reynolds-number model and requires a mesh with a properly resolved boundary-layer region (O(y+) ˜1). An overview on the grid sizes for the different configurations is given in table 6. Number of grid points vary from several hundreds of thousands for the 2D model to several million for the 3D models. A visualization of the grid on the symmetry plane and vehicle surface of the 3D models is shown in figure 8 for the CAL1B aeroshape. Grid refinement is applied to the near vehicle volumes and in the area of the plume. The nominal thermo-chemistry model for this study is based on a two species frozen gas model (frozen at nozzle exit) as described in 3.3. All heat flues are given in Terms of Nusselt number (Nu) based on aeroshell wall temperature and engine chamber temperature for reference temperature (compare table 2).

Table 6: Grid information.

Aeroshape	Configuration	Number of grid points	Symmetry
generic	UFO (2D)	3.6 x 10^5	1 degree 2D slice
CAL1B	UFO	5.6 x 10^6	half symmetry
CAL1B	UUO	9.1 x 10^6	half symmetry
CAL1C	UFO	23 x 10^6	full 3D
CAL1C	UUO	23 x 10^6	full 3D

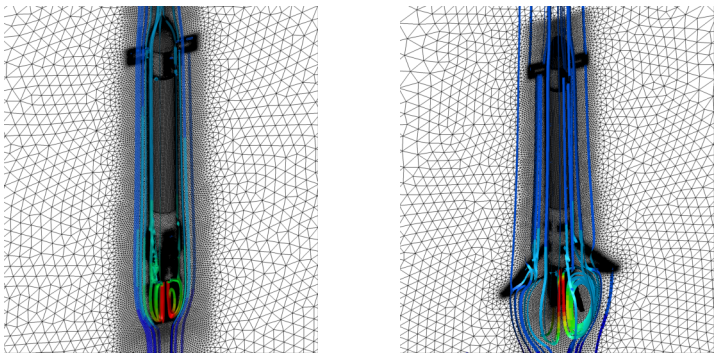

(a) UFO configuration (b) UUO configuration

Figure 8: Visualization of the grids used for CAL1B.

4.2 Phase B

Due to the large parameter space of the landing approach, the basis of the aerothermal database originates from 2D computations. Based on the different configurations the database is refined using more detailed high fidelity 3D computations, especially at points where 3D flow effects play a major role. The two-dimensional calculations build the foundation for the database and allow to cover a large and equal spaced parameter space in terms of density, Mach number and wall temperatures. A variation of generic trajectories depicting the landing approach show the crucial section of the flight corridor. More information on mission design and the approach and landing system can be found in Desmariaux et al.[5].

At the points close to the majority of sample trajectories calculations in 3D UFO configuration were performed. In the flight domain were both legs closed and legs open configurations are possible, both 3D UFO and 3D UUO configuration are considered for computations. The flight domain and calculation matrix chosen for the aerothermal load estimation for phase B is shown in figure 9. All colored trajectories marked within this figure are used in the same color scheme for the subsequent on-trajectory analyses.

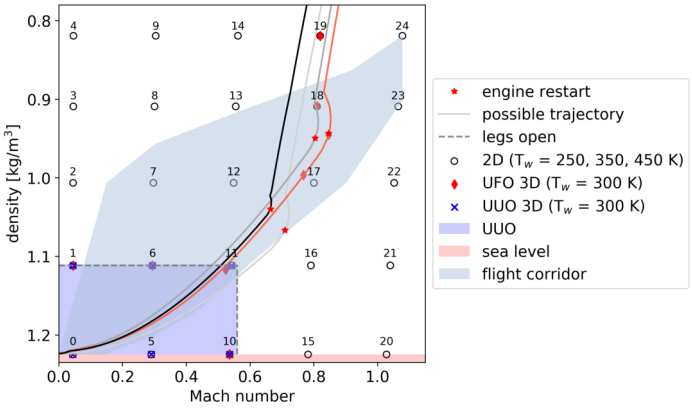

Figure 9: Calculation matrix. Phase B and using 1976 Standard Atmosphere.

4.2.1 Database generation phase B

The phase B aerothermal database is based on 75 2D CFD calculations and 13 high fidelity 3D CFD calculations, all performed for 180 deg AoA.

The final database is assembled as follows:

1. 2D calculations are used as first support points for all conditions (density and Mach number and temperature)
2. UFO 3D calculations replace selected 2D support points.
3. A second database is generated where UFO 3D points are replaced by UUO 3D points. This second database is used to evaluate conditions with open legs using linear interpolation.
4. Wall temperature influence on wall heat flux at the 3D conditions is estimated by applying the 2D gradient (dQ/dT) to the 3D condition.

4.2.2 Evaluation of integral loads and aerosphape dimensionality

The the integral rate of heat flow at all database points is shown in figure 10. The area averaged heat flux is largely dependent on relative Mach number and density. The convective heat flux scales with Mach number and density, and reaches the maximum values at high relative Mach numbers and densities. The sample trajectories indicate the main region of interest. The star markers mark the moment of engine retro boost start and are in the Mach number region of between 0.5 and 0.85 with integral rates of heat flow of up to 2.5 MW at the moment of engine ignition. Generally it can be differentiated between trajectories with ignition at relatively low Mach numbers and high atmospheric density (low altitude) and ignition at higher Mach numbers and low densities - both scenarios lead to approximately same order of magnitude of initial integral heat loads. The underlying trajectory design is related to a complex optimization process limited by thermal loads, structural loads, site regulations and demonstration flight objectives [5, 33] and will not be further discussed in this study.

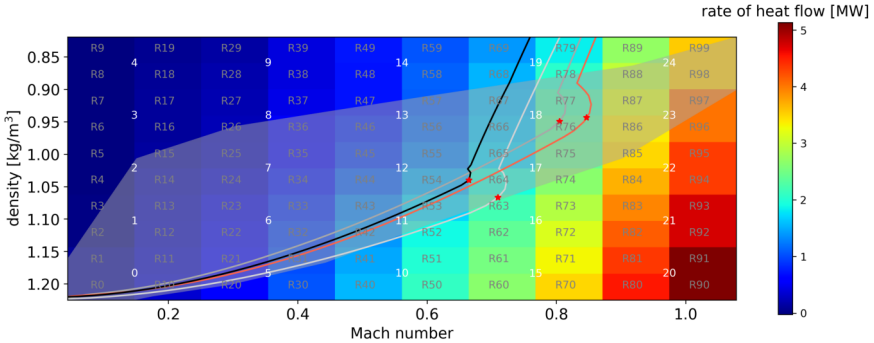

Figure 10: Integral heat transfer rate on aft bay based on 2D results (T_W = 300 K).

In order to evaluate the database and the influence of the different 2D/3D configurations the integral rate of heat flow and heat uptake along the different trajectories is estimated. Here the integral heat flow is the heat flux integrated

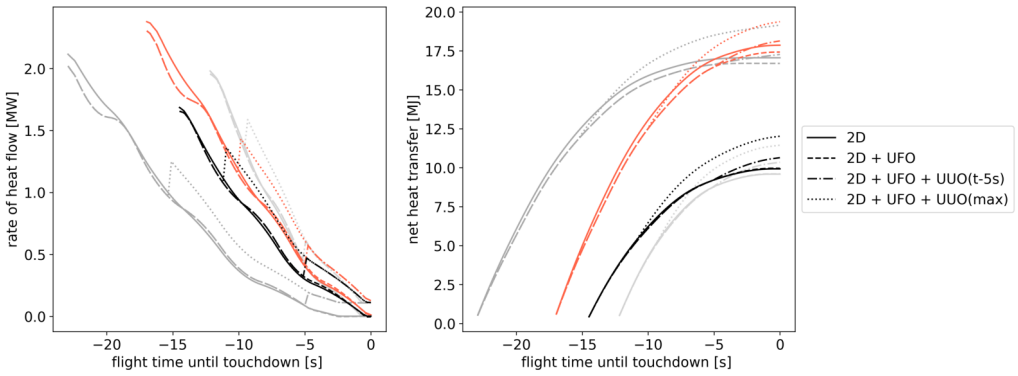

(a) integral heat transfer rate into vehicle

(b) integral heat energy transferred into vehicle

Figure 11: Integral thermal loads assuming constant wall temperature (T_W = 300 K) for several different landing trajectories. Shown trajectories refer to trajectories shown in figure 9.

over the area of the vehicle, while the heat uptake is the integral heat flow integrated over time - representing the heat uptake of the vehicle, assuming no losses due to radiation or wall temperature variation. The (area) integral rate of into the vehicle is shown in figure 11a for both 2D and 2D/3D databases. Two observations can be made: first, the maximum rate of heat flow varies significantly between trajectories, between 2 MW and 2.6 MW (for 2D database), secondly the difference between the purely 2D database and the 2D/3D database is rather small.

4.2.3 Impact on local loads

The average local loads on selected thermal interfaces are shown in figure 12. Both results for pure 2D, as well as resulting taking into account 3D effects are shown. Especially for interfaces close to the aft end and with dimensions close to 2D axisymmetric shape (e.g the baseplate) only minimal differences between 2D and 3D (2D + 3D UFO) data is observed.

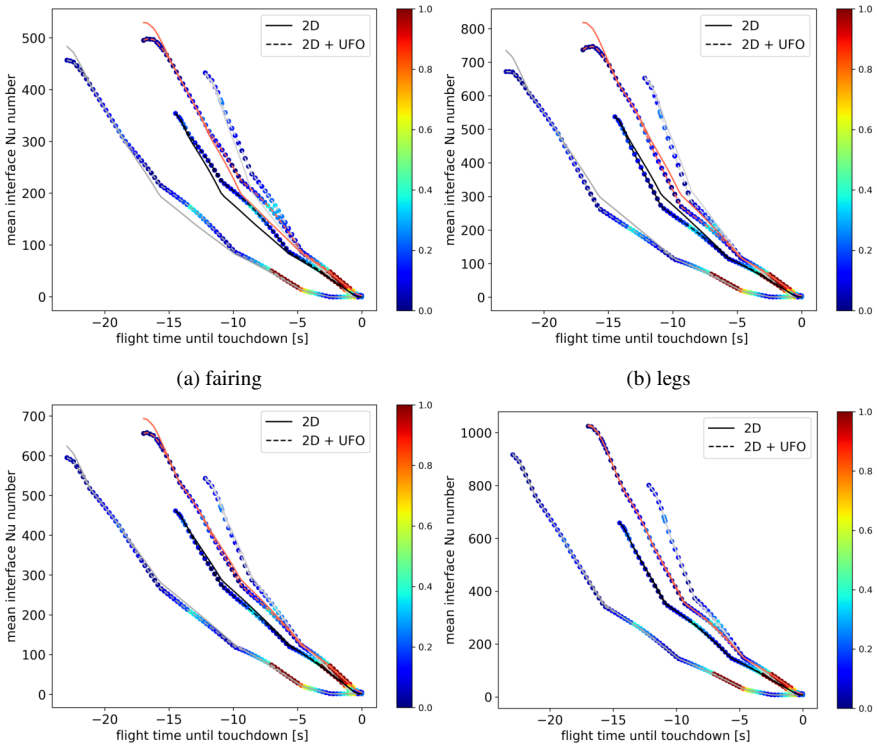

(a) fairing

(b) legs

(c) aft bay

(d) baseplate

Figure 12: Comparison of local heat flux during representative trajectory (T_W = 300 K). Filled circle indicates the goodness of fit/distance to database support point. Shown trajectories refer to trajectories shown in figure 9.

4.2.4 Estimate of interpolation errors

The errors due to database point spacing/scarcity and interpolation are estimated by comparing the CAL1B interpolated database (based on 2D data only) heat flux with values obtained on points that are directly located on the representative trajectory (see figure 2). A comparison between the heat fluxes from the flight aerothermal database, its support points and the results from the landing aerothermal database for both the fairing and the baseplate are shown in figure 14. It can be seen that the relative errors at conditions of high heat flux are fairly small, approx. between 5 to 10% (Support points 1–3) but increase quickly as the average thermal load the vehicle encounters is dropping rapidly towards the end of the trajectory. Averaged over all interfaces the max absolute error in Nu number is between 25 and 100 for all support points (compare fig 15). For phase C the 2D and 3D data spacing was reduced, which should lead to smaller interpolation errors.

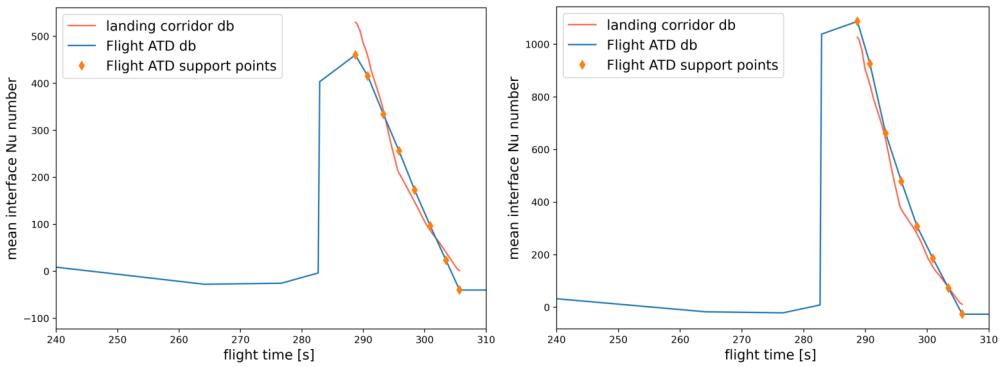

(a) fairing (b) baseplate

Figure 13: Comparison between interface heat flux predicted from landing corridor database and flight aerothermal database (representative trajectory) (T_W = 300 K).

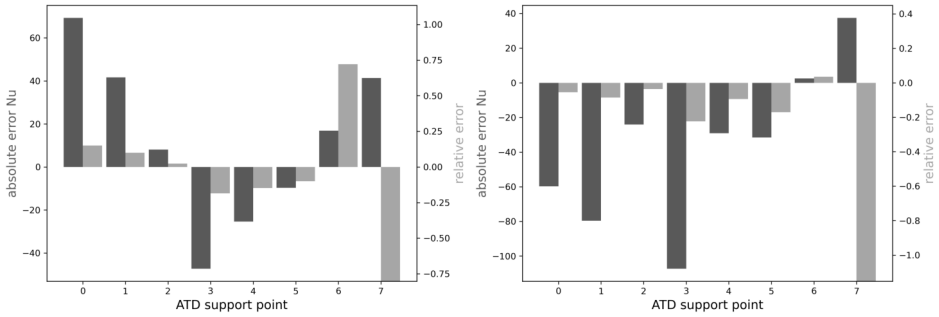

(a) fairing (b) baseplate

Figure 14: Absolute and relative errors on ATD points. (T_W = 300 K).

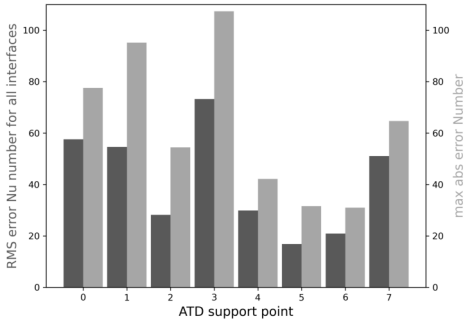

Figure 15: RMS and max error on all interfaces (T_W = 300 K).

4.3 Influence of angle of attack

The effect of angle of attack was investigated at conditions close to database points 17 and 18 (compare figure 9). The overall total rate of heat flow as a function of the angle of attack is shown in figure 16 for the UFO configuration. Generally speaking the maximum rate of heat flow into the vehicle is highest at 180 deg angle of attack. However, looking at the spatial distribution, varying the angle of attack can have a significant impact on the local heating.

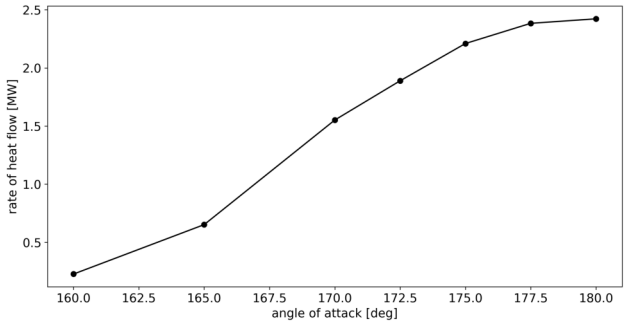

Figure 16: Integral heat transfer rate on UFO configuration at varying angle of attack (T_W = 300 K, M = 0.8).

The surface distribution of the heat flux for varying angles are shown in figure 17. At 180 deg angle of attack equal heating due to the plume-vehicle interaction is present. Changing the angle of attack to 175 deg increases the thermal loads on aft bay, tanks and fin section due to plume impingement on the vehicle. At larger angles of attack the thermal loads are concentrated on the aft bay section as a majority of the plume is diverted into the free stream and does not interact with the vehicle. The averaged heat fluxes on the thermal interfaces are shown in figure 18, showing the same aforementioned trends. The influence of the angle of attack was not included in the aerothermal database but the results prompted to include this variable for the phase C database.

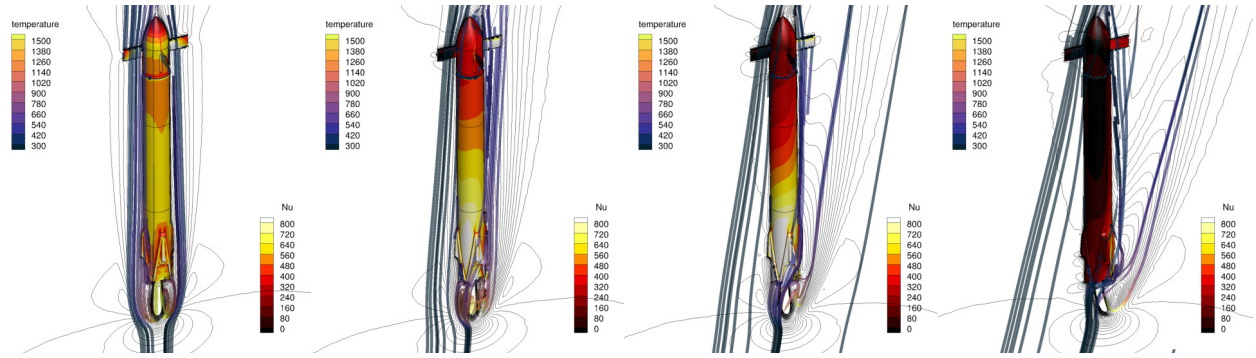

(a) 180 deg (b) 175 deg (c) 170 deg (d) 165 deg

Figure 17: Heat flux on UFO configuration at varying angle of attack (T_W = 300 K).

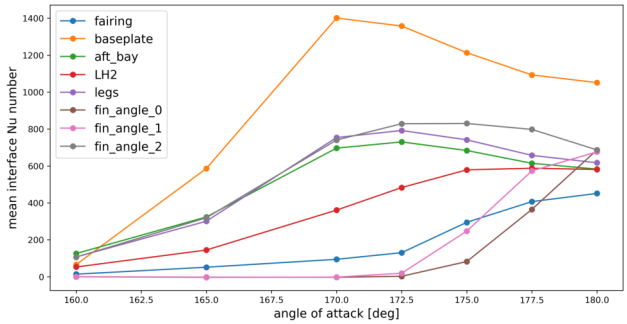

Figure 18: Heat flux on UFO configuration at varying angle of attack (T_W = 300 K, M = 0.847, $\rho = 0.9455 kg/m^3$).

4.4 Phase C

The flight domain and calculation matrix chosen for the aerothermal load estimation for phase C is shown in figure 19. The number of CFD computations for phase C is increased due to larger parameter space covering a larger envelope of return flight options. Additionally the asymmetric cable and duct components on CAL1C aeroshape require full 3D computations compared to phase B where half symmetry could be assumed. Further for CAL1B aerothermal data the 1976 Standard Atmosphere was used, while for CAL1C aerothermal data the Guiana Space Centre (CSG) atmosphere data relevant for the test and demo flights were used. This change resulted in an overall lower mean heatflux due to differences in ambient gas temperatures.

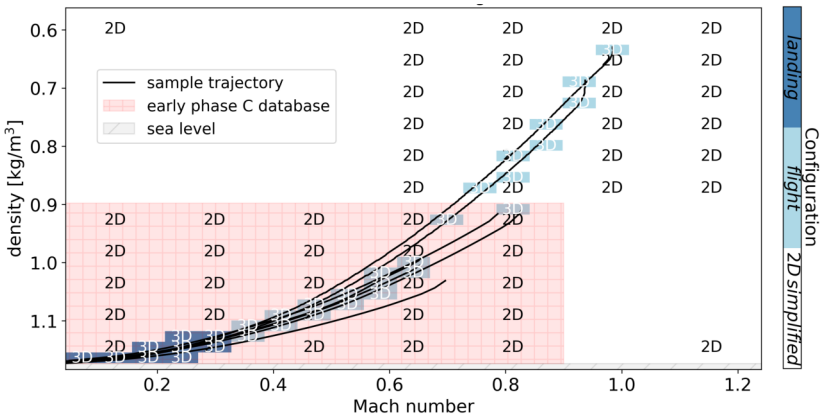

Figure 19: Calculation matrix. Phase C and using CSG atmosphere.

4.4.1 Database generation phase C

The phase C aerothermal database is based on 153 2D CFD calculations and 30 high fidelity 3D CFD calculations, all performed for 180 deg AoA. Additionally multiple calculations both for UFO and UUO at different angles of attack were performed. The final database (compare figure 19) is assembled as follows:

1. 2D calculations are performed as support points for a wide range of conditions (density and Mach number and temperature). Each support point calculation is performed for 3 different wall termperatures.
2. 3D calculations are performed on a finer grid close to possible trajectory flight points at a wall temperature of 300 K.
3. A study of selected AoA is performed for each 3D configuration at a single selected reference trajectory point at a wall temperature of 300 K.

The heat flux distribution at any given trajectory point (M, ρ, α, T_w) for each data point on each interface can then be found by evaluating the following relation:

$$Q(M,\rho,\alpha,T_w) = \Bigg[\underbrace{Q(M_i,\rho_i,180deg,300K)}_{C1} + \underbrace{\Delta Q(AoA)}_{C2}\,\underbrace{\overline{Q_i(180deg)}}_{C3}\Bigg]\underbrace{K}_{C4} + \underbrace{(dQ/dT)_{2D}(300K - T_w)}_{C5} \tag{2}$$

The single terms from left to right (C1–C5) are:
The 3D data at the closest trajectory point to the chosen evaluation point (M, ρ, α, T_w):

$$Q(M_i,\rho_i,180deg,300K) \tag{C1}$$

where the subscript i refers to the nearest 3D data point.

The AoA dependency is based on the difference between the heat flux at 180 deg AoA and the selected angle, normalized by the mean interface heatflux at this trajectory point:

$$\Delta Q(AoA) = \Delta Q(M_a,\rho_a,\alpha,300K)/\overline{Q(M_a,\rho_a,180deg,300K)} \tag{C2}$$

where

$$\Delta Q(M_a, \rho_a, \alpha, 300K) = Q(M_a, \rho_a, \alpha, 300K) - Q(M_a, \rho_a, 180deg, 300K) \tag{3}$$

and the subscript a refers to AoA data at a reference UFO/UUO trajectory point and the mean interface heat flux is defined as follows:

$$\overline{Q_i(180deg)} = \overline{Q(M_i, \rho_i, 180deg, 300K)} \tag{C3}$$

In order to account for the wide range of conditions the data is scaled based on the 2D data with a scaling factor. This scaling factor is the ratio of the mean interface heat flux of the evaluated interpolated trajectory point to mean interface heat flux of the nearest (3D data) trajectory point:

$$K = \overline{Q_{2D}(M, \rho, 180deg, 300K)} / \overline{Q_{2D}(M_i, \rho_i, 180deg, 300K)} \tag{C4}$$

Finally the wall temperature influence on wall heat flux is estimated by applying the interpolated 2D gradient (dQ/dT), which is based on three wall temperatures to the chosen evaluation point 3D conditions:

$$(dQ/dT)_{2D}(300K - T_w) \tag{C5}$$

For systems engineering purposes the heat flux distribution is averaged for each interface and saved to a database file. This database creation method was chose as it is very robust and should minimize additional uncertainties due to interpolation artifacts.

4.4.2 Local loads during flight

The local loads on selected interfaces are shown in figure 20 for both CAL1B and CAL1C databases. While for CAL1B aerothermal data the 1976 Standard Atmosphere was used, CAL1C aerothermal data assumes Guiana Space Centre (CSG) atmosphere data relevant for the test and demo flights. The change in atmosphere profile was also applied to the relevant trajectory data. This change resulted in an generally overall lower mean heatflux due to differences in ambient gas temperatures. However, due to higher ground ambient temperatures higher loads are seen right before touchdown.

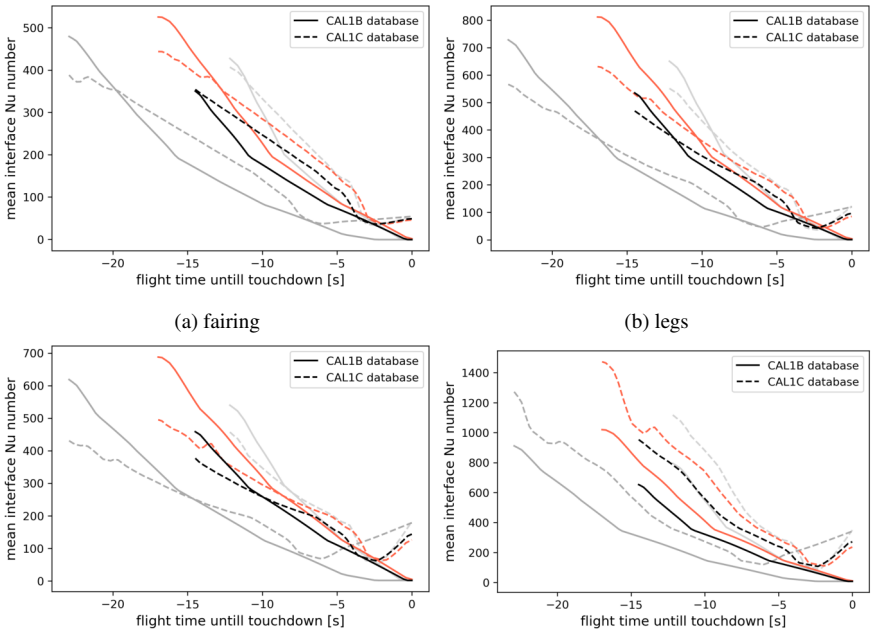

(a) fairing

(b) legs

(c) aft bay

(d) baseplate

Figure 20: Comparison of CAL1B database and CAL1C database for selected trajectories (UFO configuration). Shown trajectories refer to trajectories shown in figure 9.

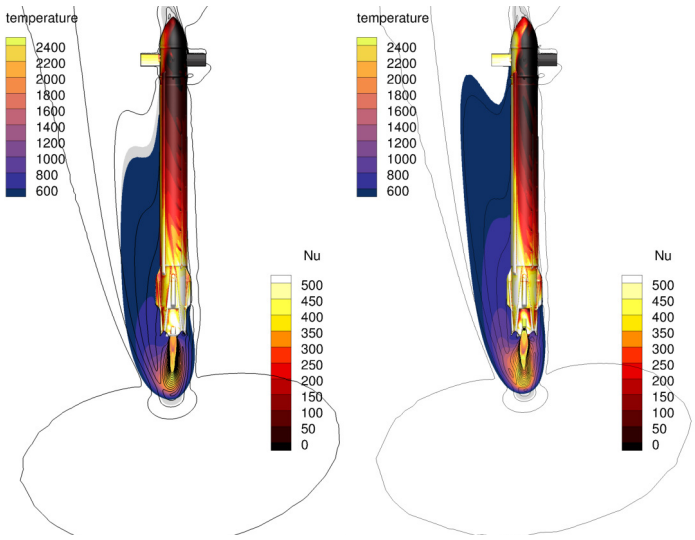

(a) 170 deg (nominal) (b) 170 deg (chemical)

Figure 21: Heat flux on UFO configuration for nominal and chemically reactive plume (T_W = 300 K, M = 0.8, $\rho = 0.72065 kg/m^3$).

4.4.3 Special cases

Special cases not covered in the aerothermal database are shown for the UFO configuration in the following figures for the impact of chemistry, thrust vector control and throttle level.

For 170 deg angle of attack the influence of post combustion chemistry is visualized in figure 21. While the load distribution is similar, differences in local loads, slightly lower loads on the aft bay region and slightly higher loads on the fin and fairing can be observed at these flight conditions. Similar to the 2D preparatory studies presented in the beginning slightly higher gas temperatures are present within the core and past the aft. This results in the higher thermal loads sensed by the downstream interfaces.

The effect of thrust vector deflection (5 deg thrust vector) on the thermal loads and the plume deflection are compared to reference conditions in figure 22. While there a local changes present, leading to higher thermal loads towards the general load cases are roughly comparable to to a case without TVC adjusted for the effective wind angle (similar to adjustment in aerodynamic forces[21]). Further analysis is required to quantify the added uncertainty from using such an approximation.

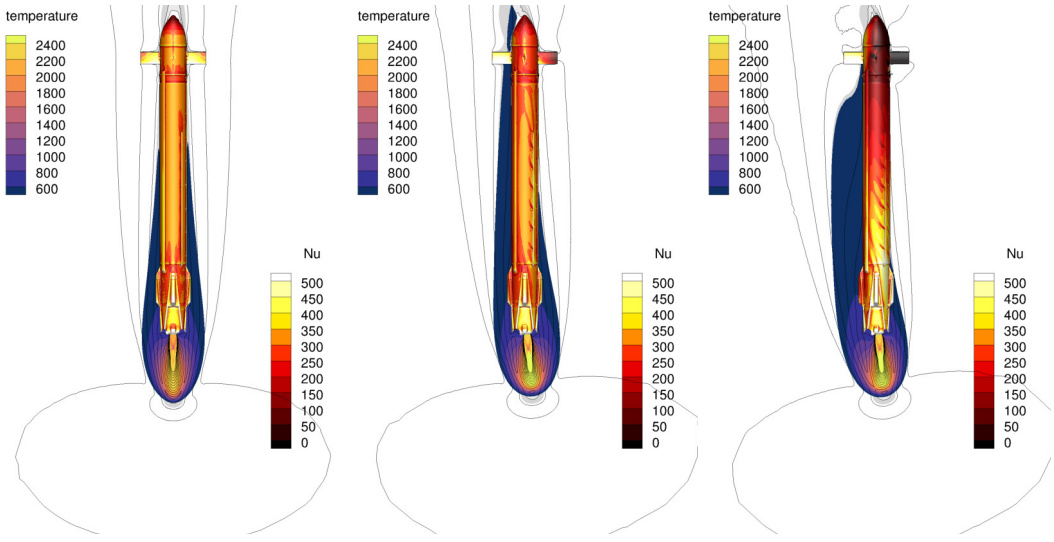

(a) 180 deg (nominal) (b) 175 deg (5 deg TVC) (c) 170 deg (5 deg TVC)

Figure 22: Heat flux on UFO configuration for nominal and TVC deflection (T_W = 300 K, M = 0.8, $\rho = 0.72065 kg/m^3$).

The effect of engine throttling is visualized in figure 23. Reducing engine thrust, respectively reducing engine mass flow rate leads to a direct reduction in heat fluxes on all interfaces.

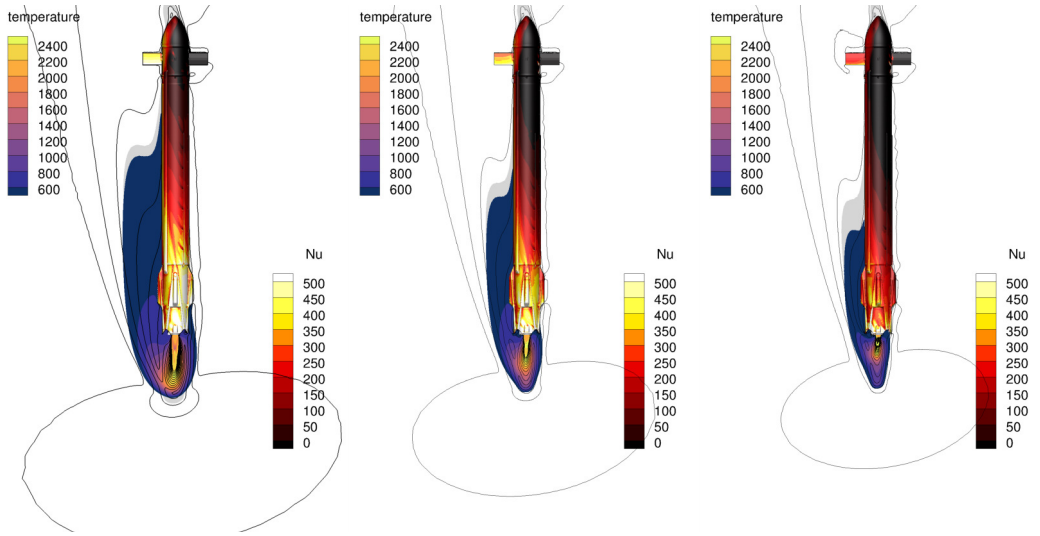

(a) 170 deg (nominal) (b) 170 deg (40% thrust) (c) 170 deg (20% thrust)

Figure 23: Heat flux on UFO configuration for varying thrust level (T_W = 300 K, M = 0.8, $\rho = 0.72065 kg/m^3$).

5. Summary

Aerothermal loads are a design driving factor during launcher development as the thermal loads directly influence thermal protection system design and trajectory. For the purpose of characterizing the aerothermal properties and loads of the CALLISTO vehicle during the design cycle, aerothermal databases are generated periodically based on current aeroshape and flight domain. In this study the CALLISTO general flight profile, vehicle configuration, and the relevant thermal interfaces are described for both phase B (CAL1B) and C (CAL1C) aeroshapes. Additionally the flight domain which defines the numerical effort is minutely detailed. Due to the large parameter space of the landing approach, the basis of the aerothermal database originates from 2D computations and is refined using more detailed high fidelity 3D computations near the critical trajectory points. The database development for vehicle phase B and phase C are described and analyzed for some of the most prominent interfaces. Due to the collaborative nature of the CALLISTO design process loads definition and respective thermal interfaces (tanks, legs, etc.) for the entire vehicle are defined. While the CAL1B aeroshape had 15 thermal interfaces, the number of interfaces for the CAL1C aeroshape had more than 50 thermal interfaces due to is detailed description involving no symmetry and many of the final mechanical extensions (cable ducts, pipes, etc.). While the phase B aerothermal database is based on 75 2D CFD calculations and 13 high fidelity 3D CFD calculations, the extend of the phase C aerothermal database was tripled to 153 2D CFD calculations and more than 40 high fidelity 3D CFD while the number of grid points increased equally. Studies of the phase B database showed that for interfaces close to the aft end and with dimensions close to 2D axisymmetric shape (e.g the baseplate) only minimal differences between 2D and 3D data is observed near 180 deg AoA. Interpolation errors for a coarse trajectory were estimated to be approx. between 5 to 10% (support points 1–3) at trajectory points with high thermal loads but also increase quickly as the average thermal load the vehicle encounters is dropping rapidly towards the end of the trajectory. Finding the angle of attack can have a significant impact on the local heating during a phase B study which prompted to include this parameter as an independent variable for the phase C database. The final phase C database presented allows interpolation of interface heatfluxes for the entire flight domain at varying angle of attack (between 180 deg and 160 deg). Further the sensitivity of the plume-vehicle interaction to angle of attack, chemistry, thrust vector deflection and engine throttling are investigated for a critical Mach number (close to max. Mach number for engine restart) indicating further area of improvement for future databases.

References

[1] J.-P. Préaud, S. Dussy, J. B. Breteau, and J. B. Bru. "Preparing the Future of European Space Transportation: Reusable Technologies and Demonstrators". In: *8th European Conference for Aeronautics and Space Sciences (EUCASS), Madrid, Spain*. July 2019. DOI: 10.13009/EUCASS2019-973.

[2] E. Dumont, S. Ishimoto, P. Tatiossian, J. Klevanski, B. Reimann, T. Ecker, L. Witte, J. Riehmer, M. Sagliano, S. G. Vincenzino, I. Petkov, W. Rotärmel, R. Schwarz, D. Seelbinder, M. Markgraf, J. Sommer, D. Pfau, and H. Martens. "CALLISTO: A Demonstrator for Reusable Launcher Key Technologies". In: *Trans. JSASS Aerospace Tech. Japan* 19.1 (2021), pp. 106–115. DOI: 10.2322/tastj.19.106.

[3] E. Dumont, S. Ishimoto, M. Illig, M. Sagliano, M. Solari, T. Ecker, H. Martens, S. Krummen, J. Desmariaux, Y. Saito, M. Ertl, J. Klevanski, B. Reimann, S. Woicke, R. Schwarz, D. Seelbinder, M. Markgraf, J. Riehmer, B. Braun, and M. Aicher. "CALLISTO: towards reusability of a rocket stage: current status". In: *33rd ISTS Conference*. Mar. 2022. URL: https://elib.dlr.de/185543/.

[4] S. Krummen, J. Desmariaux, Y. Saito, M. Boldt, L. E. Briese, N. Cesco, C. Chavagnac, E. Cliquet-Moreno, E. Dumont, T. Ecker, S. Eichel, M. Ertl, S. Giagkozoglou, T. Glaser, C. Grimm, M. Illig, S. Ishimoto, J. Klevanski, N. Lidon, O. Mierheim, J.-F. Niccolai, S. Reershemius, B. Reimann, J. Riehmer, M. Sagliano, H. Scheufler, A. Schneider, S. Schröder, R. Schwarz, D. Seelbinder, M. Stief, J. Windelberg, and S. Woicke. "Towards a Reusable First Stage Demonstrator: CALLISTO - Technical Progresses & Challenges". In: *72th International Astronautical Congress (IAC)*. IAC-21-D2.6.1. Dubai, United Arab Emirates, Oct. 2021.

[5] J. Desmariaux, E. CLIQUET-MORENO, C. Chavagnac, E. Dumont, and Y. Saito. "CALLISTO: Its Flight Envelope and Vehicle Design". In: *8th European Conference for Aeronautics and Space Sciences (EUCASS), Madrid, Spain*. July 2019. URL: https://elib.dlr.de/133317/.

[6] T. Ecker, S. Karl, E. Dumont, S. Stappert, and D. Krause. "Numerical Study on the Thermal Loads During a Supersonic Rocket Retropropulsion Maneuver". In: *Journal of Spacecraft and Rockets* 57.1 (Jan. 2020), pp. 131–146. DOI: 10.2514/1.A34486.

[7] T. Ecker, F. Zilker, E. Dumont, S. Karl, and K. Hannemann. "Aerothermal Analysis of Reusable Launcher Systems during Retro-Propulsion Reentry and Landing". In: *Space Propulsion Conference 2018*. May 2018. URL: https://elib.dlr.de/120072/.

[8] M. Laureti and S. Karl. "Aerothermal databases and load predictions for Retro Propulsion-Assisted Launch Vehicles (RETALT)". In: *CEAS Space Journal* (2022), pp. 1–15. DOI: 10.1007/s12567-021-00413-0.

[9] E. Dumont, T. Ecker, C. Chavagnac, L. Witte, J. Windelberg, J. Klevanski, and S. Giagkozoglou. "CALLISTO - Reusable VTVL launcher first stage demonstrator". In: *Space Propulsion Conference 2018*. May 2018. URL: https://elib.dlr.de/119728/.

[10] P. Reijasse and J. Delery. "Investigation of the flow past the ARIANE 5 launcher afterbody". In: *Journal of Spacecraft and Rockets* 31.2 (1994), pp. 208–214. DOI: 10.2514/3.26424. eprint: https://doi.org/10.2514/3.26424. URL: https://doi.org/10.2514/3.26424.

[11] O. Kramer. "Evaluation of thermal radiation from the Titan III solid rocket motor exhaust plumes". In: *5th Thermophysics Conference*. 1970. DOI: 10.2514/6.1970-842. eprint: https://arc.aiaa.org/doi/pdf/10.2514/6.1970-842. URL: https://arc.aiaa.org/doi/abs/10.2514/6.1970-842.

[12] T. F. Greenwood, Y. C. Lee, R. L. Bender, and R. E. Carter. "Space Shuttle base heating". In: *Journal of Spacecraft and Rockets* 21.4 (1984), pp. 339–345. DOI: 10.2514/3.25660. eprint: https://doi.org/10.2514/3.25660. URL: https://doi.org/10.2514/3.25660.

[13] J. Vila and J. Hassin. "Technology acceleration process for the THEMIS low cost and reusable prototype". In: *8th European Conference for Aeronautics and Space Sciences (EUCASS), Madrid, Spain*. July 2019. DOI: 10.13009/EUCASS2019-97.

[14] A. Iannetti, N. Girard, N. Ravier, E. Edeline, and D. Tchou-Kien. "PROMETHEUS, a low cost LOX/CH4 engine prototype". In: *53rd AIAA/SAE/ASEE Joint Propulsion Conference*. DOI: 10.2514/6.2017-4750. eprint: https://arc.aiaa.org/doi/pdf/10.2514/6.2017-4750. URL: https://arc.aiaa.org/doi/abs/10.2514/6.2017-4750.

[15] A. P. de Mirand, J.-M. Bahu, and O. Gogdet. ""Ariane Next, a vision for the next generation of Ariane Launchers"". In: *"Acta Astronautica"* ("2020"). ISSN: "0094-5765". DOI: "https://doi.org/10.1016/j.actaastro.2020.02.003",31".

[16] T. Ecker, S. Karl, E. Dumont, S. Stappert, and D. Krause. "A Numerical Study on the Thermal Loads During a Supersonic Rocket Retro-Propulsion Maneuver". In: *53rd AIAA/SAE/ASEE Joint Propulsion Conference*. 2017. URL: https://elib.dlr.de/111762/.

[17] E. Dumont, S. Stappert, T. Ecker, J. Wilken, S. Karl, S. Krummen, and M. Sippel. "Evaluation of Future Ariane Reusable VTOL Booster stages". In: *68th International Astronautical Congress*. IAC-17-D2.4.3. Sept. 2017. URL: https://elib.dlr.de/114430/.

[18] M. Ertl, T. Ecker, J. Klevanski, S. Krummen, and E. Dumont. "Aerothermal analysis of plume interaction with deployed landing legs of the CALLISTO vehicle". In: *9th European Conference for Aeronautics and Space Sciences*. 2022.

[19] J. Klevanski, T. Ecker, J. Riehmer, B. Reimann, E. Dumont, and C. Chavagnac. "Aerodynamic Studies in Preparation for CALLISTO - Reusable VTVL Launcher First Stage Demonstrator". In: *69th International Astronautical Congress (IAC)*. IAC-18- D2.6.3. Oct. 2018. URL: https://elib.dlr.de/122062/.

[20] T. Sivignon, J. Caillaud, and J. Desmariaux. "Control law design for the Callisto demonstrator". In: *8th European Conference for Aeronautics and Space Sciences (EUCASS), Madrid, Spain*. July 2019. DOI: 10.13009/EUCASS2019-216.

[21] J. Klevanski, B. Reimann, S. Krummen, M. Ertl, T. Ecker, J. Riehmer, and E. Dumont. "Progress in Aerodynamic Studies for CALLISTO - Reusable VTVL Launcher First Stage Demonstrator". In: *9th European Conference for Aeronautics and Space Sciences*. 2022.

[22] S. G. Vincenzino, S. Eichel, W. Rotärmel, F. Krziwanie, I. Petkov, E. Dumont, A. Schneider, S. Schröder, J. Windelberg, T. Ecker, and M. Ertl. "Development of Reusable Structures and Mechanisms for CALLISTO". In: *33rd ISTS Conference*. Mar. 2022. URL: https://elib.dlr.de/185598/.

[23] S. Langer, A. Schwöppe, and N. Kroll. "The DLR Flow Solver TAU – Status and Recent Algorithmic Developments". In: *AIAA Paper AIAA-2014-0080*. 52nd Aerospace Sciences Meeting (2014). DOI: 10.2514/6.2014-0080.

[24] M. Sato, T. Hashimoto, S. Takada, T. Kimura, T. Onodera, Y. Naruo, T. Yagishita, K.-I. Niu, T. Kaneko, and K. Obase. "Development of Main Propulsion System for Reusable Sounding Rocket: Design Considerations and Technology Demonstration". In: *TRANSACTIONS OF THE JAPAN SOCIETY FOR AERONAUTICAL AND SPACE SCIENCES, AEROSPACE TECHNOLOGY JAPAN* 12 (Jan. 2014). DOI: 10.2322/tastj.12.Tm_1.

[25] T. Kimura, T. Hashimoto, M. Sato, S. Takada, S.-i. Moriya, T. Yagishita, Y. Naruo, H. Ogawa, T. Ito, K. Obase, and H. Ohmura. "Reusable Rocket Engine: Firing Tests and Lifetime Analysis of Combustion Chamber". In: *Journal of Propulsion and Power* 32.5 (2016), pp. 1087–1094. DOI: 10.2514/1.B35973.

[26] S. Ishimoto, P. Tatiossian, and E. Dumont. "Overview of the CALLISTO Project". In: *32nd ISTS and NSAT*. June 2019. URL: https://elib.dlr.de/132886/.

[27] T. Kimura, T. Hashimoto, M. Sato, S. Takada, S.-i. Moriya, T. Yagishita, Y. Naruo, H. Ogawa, T. Ito, K. Obase, and H. Ohmura. "Reusable Rocket Engine: Firing Tests and Lifetime Analysis of Combustion Chamber". In: *Journal of Propulsion and Power* 32 (Apr. 2016), pp. 1–8. DOI: 10.2514/1.B35973.

[28] V. Hannemann. *Numerical simulation of shock-shock-interactions considering chemical and thermal nonequilibrium*. DLR-Forschungsbericht 97-07, 1997.

[29] P. Gerlinger, H. Moebius, and D. Brueggmann. "An Implicit Multigrid Method for Turbulent Combustion". In: *Journal of Computational Physics* 167.2 (2001), pp. 247–276. ISSN: 0021-9991. DOI: 10.1006/jcph.2000.6671.

[30] S. Gordon and B. J. McBride. *Computer Program for Calculation of Complex Chemical Equilibrium Compositions and Applications*. Tech. rep. NASA Reference Publication 1311, 1996.

[31] Spalart, P.R. and Allmaras, S.R. "A One-Equation Turbulence Model for Aerodynamic Flows". In: *AIAA Paper AIAA-92-0439* (1992). DOI: 10.2514/6.1992-439.

[32] L. Eça, M. Hoekstra, A. Hay, and D. Pelletier. "A manufactured solution for a two-dimensional steady wall-bounded incompressible turbulent flow". In: *International Journal of Computational Fluid Dynamics* 21.3-4 (2007), pp. 175–188. DOI: 10.1080/10618560701553436. eprint: https://doi.org/10.1080/10618560701553436. URL: https://doi.org/10.1080/10618560701553436.

[33] M. Sagliano, T. Tsukamoto, J. A. M. Hernandez, D. Seelbinder, S. Ishimoto, and E. Dumont. "Guidance and Control Strategy for the CALLISTO Flight Experiment". In: *8th European Conference for Aeronautics and Space Sciences (EUCASS), Madrid, Spain*. July 2019. URL: https://elib.dlr.de/128999/.